

Gravitational Waves from a Core g -Mode in Supernovae as Probes of the High-Density Equation of State

Pia Jakobus,* Bernhard Müller, and Alexander Heger
School of Physics and Astronomy, Monash University, Clayton, VIC 3800 Australia

Shuai Zha
Tsung-Dao Lee Institute, Shanghai Jiao Tong University, Shanghai 200240, China

Jade Powell
Centre for Astrophysics and Supercomputing, Swinburne University of Technology, Hawthorn, VIC 3122, Australia

Anton Motornenko, Jan Steinheimer, and Horst Stöcker
Frankfurt Institute for Advanced Studies, Giersch Science Center, Frankfurt am Main, Germany

Using relativistic supernova simulations of massive progenitor stars with a quark-hadron equation of state (EoS) and a purely hadronic EoS, we identify a distinctive feature in the gravitational-wave signal that originates from a buoyancy-driven mode (g -mode) below the proto-neutron star convection zone. The mode frequency lies in the range $200 \lesssim f \lesssim 800$ Hz and decreases with time. As the mode lives in the core of the proto-neutron star, its frequency and power are highly sensitive to the EoS, in particular the sound speed around twice saturation density.

Introduction.—Core-collapse supernovae (CCSNe) are among the most important astronomical events yet to be detected by ground-based gravitational-wave (GW) interferometers [1–5]. With current detector sensitivity, the event must occur within at most a few 10 kpc of Earth [4, 6, 7]. Future detectors, such as the Einstein Telescope, may observe supernovae throughout the Milky Way and beyond the Magellanic Clouds [8–11]. The estimated rate for galactic CCSNe is $3_{-2.6}^{+7.3}$ per century [12, 13], implying a realistic chance of detection within the lifetime of second- and third-generation instruments. Such a detection would reveal insights into the properties of the proto-neutron star and the multi-dimensional fluid flow in the supernova core. Multi-dimensional simulations [e.g., 14–25] show that the GW signal reflects the presence of proto-neutron star (PNS) oscillation modes triggered by convection, turbulent accretion, the standing-accretion shock instability (SASI) [26], or triaxial instabilities. The most robust feature in the signal comes from a quadrupolar f/g -mode [15, 21, 27–31] with a frequency that increases in time from a few hundred Hz to above 1 kHz. Future GW observations may measure this frequency [32, 33] and use mode relations [15, 34, 35] to constrain bulk PNS parameters (mass, radius, surface temperature).

Unfortunately, the dominant f/g -mode is largely confined to the PNS surface region and therefore only indirectly sensitive (through the PNS radius) to the high-density equation of state (EoS). Nevertheless, potential GW diagnostics that could also constrain the properties of nuclear matter at several times nuclear saturation density $\rho_0 \geq 2.6 \times 10^{14} \text{ g cm}^{-3}$ and temperatures of several 10 GK are being identified. The GW signal could shed light on the nuclear EoS, e.g., about the possible appear-

ance of quarks at high densities [36, 37], which is not considered in most standard CCSN simulations. A first-order phase transition from hadrons to quarks [38, 39], which is already known to strongly affect post-merger GW emission in neutron star mergers [40–43], produces a loud and distinct supernova GW signature with a peak at several kHz, regardless of whether the phase transition triggers an explosion [44–46].

Here we compare the predicted GW signals from supernova simulations with the purely hadronic SFHx EoS [47] and the chiral mean field (CMF) EoS [48] with a *smooth crossover* to quark matter. We find that the CMF models exhibit a *core g*-mode signature of lower frequency and higher intensity as a distinct GW fingerprint, and elucidate the underlying EoS properties.

Methods.—We perform axisymmetric (2D) simulations with the general-relativistic neutrino hydrodynamics code CoCoNuT-FMT [49, 50]. Different from recent multi-D simulations with CoCoNuT-FMT, we calculate only a small inner region of radius < 1380 m in spherical symmetry to capture g -modes in the PNS core. GW signals are calculated using a modified version [15] of the time-integrated quadrupole formula [51]. We use two zero-metallicity progenitors of $35 M_\odot$ and $85 M_\odot$ (named **z35** and **z85**), which are calculated with the stellar evolution code KEPLER [52, 53].

We employ two different high-density EoS. For models **z35:CMF** and **z85:CMF**, we use the CMF model with a first-order nuclear liquid-vapor phase transition at densities $\sim \rho_0$, a second, but weak first-order phase transition due to chiral symmetry restoration at $\sim 4 \times \rho_0$ with a critical endpoint at $T_{\text{CeP}} \approx 15$ MeV, and a smooth transition to quark matter at higher densities. The CMF EoS has a ground state density (for symmetric matter)

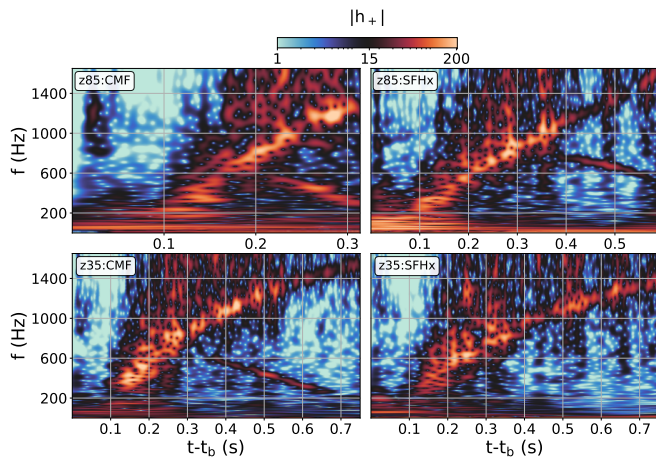


FIG. 1. GW spectrograms for **z85** (top) and **z35** (bottom) using the **CMF**-EoS (left) and **SFHx**-EoS (right). The same logarithmic color scale for the amplitude $|h^+|$ is used for all models. Models **z85:CMF**, **z85:SFHx** and **z35:CMF** exhibit a distinct second frequency band from the 2g_1 -mode, which branches off the dominant band after a few hundred milliseconds.

$n_{\text{sat}} = 0.16 \text{ fm}^{-3}$, binding energy per baryon $E_0/B = -15.2 \text{ MeV}$, asymmetry energy $S_0 = 31.9 \text{ MeV}$, incompressibility $K_0 = 267 \text{ MeV}$, and a maximum Tolman-Oppenheimer-Volkoff mass $M_{\text{TOV}}^{\text{max}} = 2.10 M_{\odot}$ [48]. This EoS has recently been studied in the context of neutron star merger and 1D CCSN simulations [54, 55]. The second EoS, used for runs **z35:SFHx** and **z85:SFHx**, is the purely hadronic relativistic mean-field **SFHx** model [47]. Nuclear matter properties for the **SFHx** EoS are: $n_{\text{sat}} = 0.16 \text{ fm}^{-3}$, $E_0/B = -16.16 \text{ MeV}$, $S_0 = 28.67 \text{ MeV}$, $K_0 = 239 \text{ MeV}$, and $M_{\text{TOV}}^{\text{max}} = 2.13 M_{\odot}$.

Results.— Dynamically, the **CMF** and **SFHx** models exhibit similar behaviour. Both **z85** models undergo shock revival followed by early black hole formation, albeit earlier by more than 0.2 s in **z85:CMF**. Both **z35** models explode. The GW signals of the **CMF** and **SFHx** models exhibit distinctive differences, however. Figure 1 shows GW spectrograms computed using the Morlet wavelet transform [56].

The early phase of GW emission is still similar for both EoSs. The **z85** models show low-frequency emission at $\sim 100 \text{ Hz}$ due to prompt convection and early SASI activity [14, 15, 57, 58]; this is largely absent in the **z35** models. Subsequently, the PNS surface f/g -mode [15, 21, 28, 29] appears as a prominent emission band with frequencies that increase from $\sim 300 \text{ Hz}$ to above 1000 Hz . The f/g -mode frequency rises slightly faster in the **CMF** models.

The most striking differences are found in another emission band of *decreasing* frequency that branches off the dominant f/g -mode between 0.2 s and 0.35 s, except in **z35:SFHx** which shows no such signal. A linear mode analysis (see [21, 29, 30, 35] for the methodology) identi-

fies this frequency band as the decreasing branch of the 2g_1 mode (Zha et al. in prep.), i.e., a quadrupolar g -mode with one node, with an eigenfunction mostly confined to the PNS core (core g -mode). Henceforth we refer to the decreasing branch as the 2g_1 mode for short¹.

The mode frequency f_{2g_1} is systematically lower in **z85:CMF** compared to **z85:SFHx**. In **z85:CMF**, f_{2g_1} decreases from $\sim 600 \text{ Hz}$ at 0.2 s to $\sim 220 \text{ Hz}$ at 0.32 s, at which point the model collapses to a BH. In **z85:SFHx**, BH collapse occurs later and f_{2g_1} evolves more slowly from a higher frequency of $\sim 800 \text{ Hz}$ down to $\sim 560 \text{ Hz}$ at 0.58 s. In **z35:CMF**, the 2g_1 mode lives at similarly low frequencies as in **z85:CMF**, i.e., in the range 220–600 Hz.

Such pronounced emission in the declining 2g_1 -mode frequency band as in the **CMF** models (and to a lesser extent model **z85:SFHx**) is not usually observed in simulations with energy-dependent neutrino transport. These usually show an emission *gap* at the avoided crossing with the f -mode [21]. The 2g_1 -mode has been found in simulations with more approximate neutrino transport [59, 60], or modified Newtonian gravity [25, 29, 34].

To further confirm the nature of the mode, we perform a spatially resolved Fourier analysis of the integrand of the quadrupole formula using high-time-resolution simulation output with sampling frequency 10^4 Hz . To detect quadrupolar motions as a function of radius and frequency, we integrate over angle only, and obtain a radius-dependent measure $q(r, t)$ of quadrupolar perturbations,

$$q(r, t) = \frac{32\pi^{3/2}G}{\sqrt{15}c^4} \int_0^\pi d\theta \phi^6 r^3 \sin\theta \times \left\{ \frac{\partial}{\partial t} (S_r(3\cos^2\theta - 1)) + \frac{3}{r} S_\theta \sin\theta \cos\theta \right\}. \quad (1)$$

ϕ is the conformal factor of the space-time metric, and S_r and S_θ are the orthonormal components of the relativistic momentum density.

We obtain spectrograms of $q(r, t)$ (Figure 2, first two panels) using the Fast-Fourier transforms (FFT) in a fixed time window Δt and apply additional denoising by convolving the FFT with a weighted sum of radial basis functions [61].

Spectrograms are shown for two time windows Δt_1 and Δt_2 around 0.4 s and 0.55 s (marked as red shaded areas in the third panel of Figure 2) for model **z35:CMF**. During Δt_1 , the spectrograms show power corresponding to the low-frequency signal at $4 \text{ km} \lesssim r \lesssim 8 \text{ km}$ and a frequency of $\sim 600 \text{ Hz}$, with a weaker “hotspot” at $\sim 500 \text{ Hz}$. Later, during Δt_2 , the hotspot is stronger and its centroid shifts towards small radii (although it still reaches

¹ The dominant band with increasing frequency follows the *increasing* branch of the 2g_1 mode initially and then the f -mode after the avoided crossing of the two modes. The mode classification is, e.g., sensitive to the boundary condition in the linear analysis.

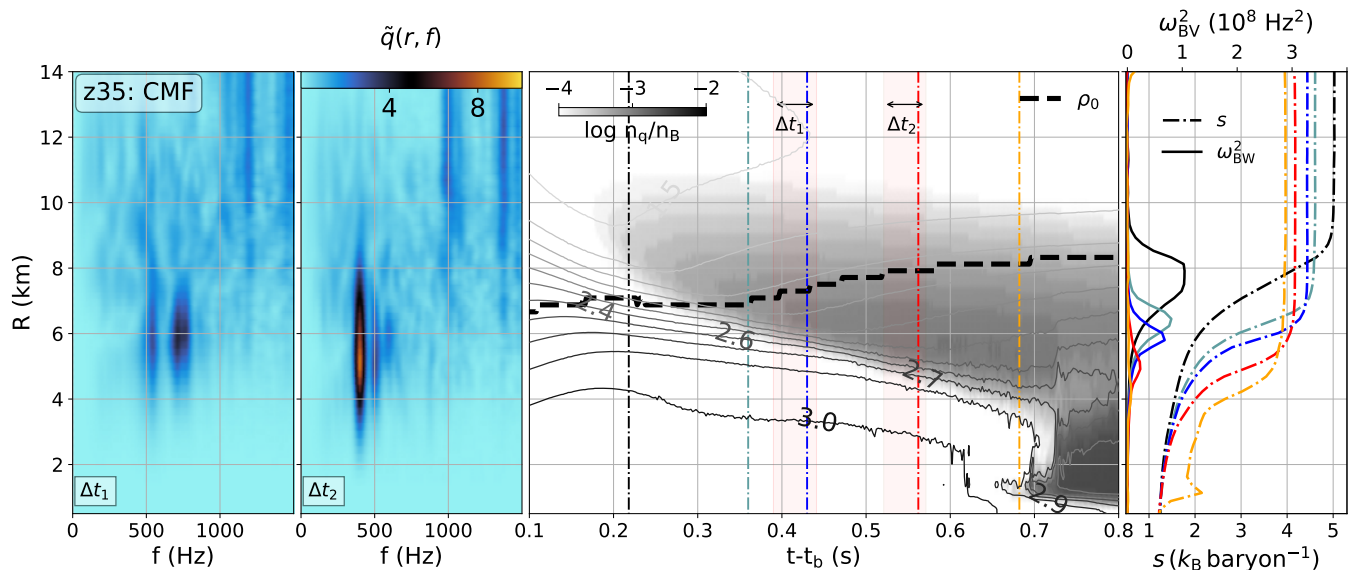


FIG. 2. *First and second panel:* Amplitude $\tilde{q}(r, f)$ of the Fourier transform of the quadrupolar perturbation $q(r, t)$ as a function of radius and frequency f for the time intervals Δt_1 and Δt_2 around 0.4 s and 0.55 s (indicated in red shades in the third panel) for model z35:CMF. *Third panel:* Color contour plot of the quark fraction n_q/n_B as a function of time and radius, combined with isocontours for the adiabatic index (solid lines in different shades of gray) and a thick black line indicating the radius corresponding to nuclear saturation density. *Fourth panel:* Brunt-Väisälä frequency ω_{BV}^2 (solid lines) and spherically averaged specific entropy per baryon s , (dashed) at five different times, which are indicated on the time axis of the third panel as vertical lines of the respective colour. The last entropy profile (orange) shows a blip at a radius of less than 2 km, which is due to a convective plume that penetrates the PNS core when the buoyancy barrier at the inner edge of the PNS convection zone is eroded ($\omega_{\text{BV}}^2 \approx 0$).

out to ~ 8 km) as the PNS contracts. The frequency decreases to ~ 430 Hz and is clearly defined. Profiles of the relativistic Brunt-Väisälä frequency ω_{BV}^2 [15] and specific entropy per baryon s (Figure 2, fourth panel) show that the mode is located at the *inner* boundary of the PNS convection zone, originating from a different region than the high-frequency emission, which is visible in two streaks above 1 kHz at larger radii. The profiles of ω_{BV}^2 also explain the downward trend in frequency as the peak in ω_{BV}^2 decreases with time. All of this strongly supports the identification as a core g -mode.

This still leaves the question why the 2g_1 -mode has a significantly lower frequency and is more strongly excited in the CMF models. Before a more quantitative analysis, it is important to note that quark formation is not *directly* responsible in the CMF models for the smaller mode frequency as evident from the time- and radius-dependent quark fraction n_q/n_B (Figure 2, third panel).

Although quarks appear off-center at $8 \text{ km} \lesssim r \lesssim 10 \text{ km}$ quite early at ~ 0.2 s, they appear only in small numbers $n_q/n_B \leq 10^{-4}$. The appearance of quarks at low densities is due to the absence of a sharp phase transition in the CMF EoS and the high temperatures in the PNS mantle, but is of little dynamical relevance. Quarks only appear more abundantly and lead to significant softening later at ~ 0.7 s at radii ~ 2 km. Thus, the full transition to quark matter comes too late to account for the

distinct 2g_1 -mode in z35:CMF as opposed to z35:SFHx well before 0.7 s.

The lower 2g_1 -mode frequency in the CMF models is rather connected to lower peaks of ω_{BV}^2 at the inner boundary of the PNS convection zone at densities below $2 \times \rho_0$ (colored solid lines in Figure 3). At late times the buoyancy barrier at the bottom of the PNS convective zone disappears almost entirely, and the entropy profiles show overshooting into the core as favourable conditions for “inverted convection” to develop [55]. The reason for the lower Brunt-Väisälä frequency can be analyzed by writing ω_{BV}^2 as

$$\omega_{\text{BV}}^2 = \frac{d\alpha}{dr} \frac{\alpha}{\rho h \phi^4} \frac{1}{c_s^2} \left[\left(\frac{\partial P}{\partial s} \right)_{\bar{\rho}, Y_e} \frac{ds}{dr} + \left(\frac{\partial P}{\partial Y_e} \right)_{\bar{\rho}, s} \frac{dY_e}{dr} \right], \quad (2)$$

and considering the impact of the various gradients and thermodynamic derivatives. Here, α is the lapse function, ρ is the baryonic mass density, $\bar{\rho}$ is the total mass-energy density, P is the pressure, $h = (\bar{\rho} + P/c^2)/\rho$ is the relativistic enthalpy, Y_e is the electron fraction, and c_s is the sound speed. The most conspicuous feature in the CMF models is a higher sound speed than in the SFHx models at the location corresponding to the maximum of ω_{BV} (color shading in Figure 3), once the inner edge of the PNS convection zone contracts to densities of about

$2 \times \rho_0$. This is due to significant stiffening of the CMF EoS owing to baryon-baryon repulsion [48]. Although not directly related to the formation of quark matter, such pronounced stiffening at moderately high densities is characteristic of currently viable EoS with a phase transition or crossover to quark matter [62–64]. The stiffening is crucial for achieving maximum neutron star masses compatible with observational constraints and tentatively supported by heavy-ion collisions [65, 66]. On top of the systematic difference in sound speed between the two EoSs, we also find a somewhat disparate PNS structure, which complicates the comparison of ω_{BV}^2 between CMF and SFHx models, e.g., the inner edge of the PNS convection zone as defined by the peak in ω_{BV} tends to lie at higher densities in the CMF models. Although the difference in sound speed has a clear impact on ω_{BV} and can be readily connected to the underlying physics of the EoS, there are further smaller effects that will eventually need to be incorporated in a rigorous theory for the EoS-dependence of the 2g_1 -mode. Differences in the electron fraction gradient dY_e/dr also contribute to the lower ω_{BV} for CMF. Different from the SFHx models, dY_e/dr becomes negative in the region of interest before the onset of the signal. With positive $(\partial P/\partial Y_e)_{\bar{\rho},s}$, the second term in brackets in Equation (2) then decreases ω_{BV} , especially since $(\partial P/\partial Y_e)_{\bar{\rho},s}$ diverges from the SFHx EoS at this point and becomes larger by up to a factor of four in the PNS core in the CMF models. The ultimate cause for the different behaviour is that the small “hump” in Y_e at a mass coordinate of $\sim 0.7 M_\odot$ that is imprinted on the PNS structure shortly after bounce is erased quicker by neutrino diffusion in the CMF models. The terms $(\partial P/\partial s)_{Y_e,\bar{\rho}}$ and ds/dr also show some EoS dependence, but their net effect is even smaller. Details are shown in the Supplementary Material.

It is more challenging to trace the higher *power* in GWs emitted by the 2g_1 -mode to the PNS structure and to EoS properties. Stronger excitation of the 2g_1 -mode in the CMF models could be due to stronger PNS convection or more efficient coupling between the forcing convective motions and the 2g_1 -mode. Stronger convection in the CMF models appears to at least play an important role. The turbulent kinetic energy in the PNS convection zone is about an order of magnitude larger in z35:CMF at several 10^{50} erg than in z35:SFHx, and still somewhat larger in z85:CMF than in z85:SFHx (see Supplementary Material). Both z85 models have significantly higher turbulent convective energies than the z35 models in line with recent findings of stronger PNS convection for more massive progenitors [67]. The higher convective energies are mostly due to higher turbulent velocities and less due to differences in the mass of the PNS convection zone. The empirical finding of stronger PNS convection in the CMF models explains the conspicuous signal from the 2g_1 -mode in the GW spectrograms, but further work is needed to identify the underlying physical reason.

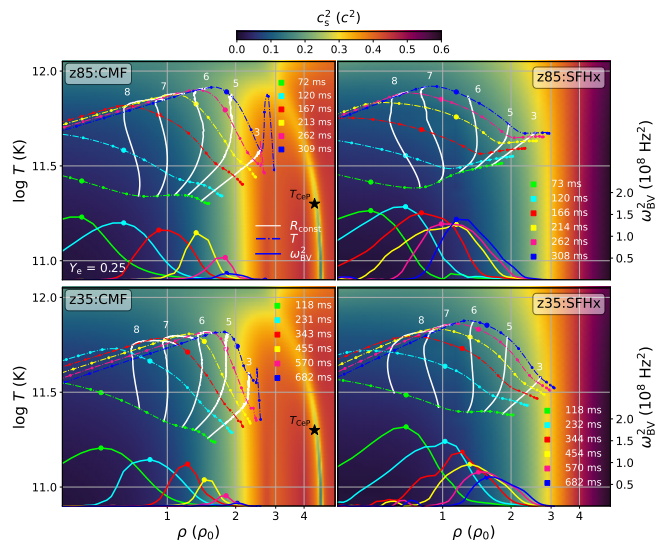


FIG. 3. Color contour plots of the squared sound speed c_s^2 as a function of density ρ and temperature T for an electron fraction of $Y_e = 0.25$ for models z85 (top) and z35 (bottom) with the CMF EoS (left), and the SFHx EoS (right). Solid and dashed curves show ω_{BV}^2 and (spherically averaged) temperature profiles $T(\rho)$ at various times (indicated by line color). The density where ω_{BV}^2 peaks is indicated by a dot on the curves. The white lines indicate five constant radii; the radius (in km) is indicated on top. Note a temperature blip at high densities due to the overshooting of plumes into the PNS at late times (blue curves) in the CMF models.

Unfortunately, the dynamics of PNS convection are not fully understood because of the complicated interplay of stabilising and destabilising stratification gradients and multi-dimensional convective flow [e.g., 10, 68–71]. It is noteworthy, however, that a significant impact of EoS properties on the long-term behaviour of PNS convection during the Kelvin-Helmholtz cooling phase has been reported before [72].

Conclusions.— Our 2D supernova simulations with a quark-hadron CMF EoS [48] and the hadronic SFHx EoS [47] show a characteristic GW emission band with *decreasing* frequencies of several hundred Hz in addition to the well-known emission band from the dominant f/g -mode. We identified a core g -mode (2g_1 -mode) that mostly lives around the inner boundary of the PNS convection zone as the oscillation mode responsible for this GW feature.

The mode frequency and power are very sensitive to the high-density EoS. For a $35 M_\odot$ progenitor, the GW signal from the 2g_1 -mode is only present for the CMF EoS, and for a $85 M_\odot$ progenitor, it is stronger, appears earlier and lies at lower frequencies for the CMF EoS. The lower frequency indicates a softening of the inner boundary of the PNS convection zone primarily due to a higher sound speed of the CMF EoS at densities of about $2 \times \rho_0$. The strength of PNS convection as a driver of the 2g_1 -mode

is sensitive to the EoS, which explains the stronger GW signal from this mode for the CMF EoS.

These results suggest that the supernova GW signal holds more promise for probing properties of nuclear matter beyond saturation density than hitherto thought because the signal from the 2g_1 -mode is determined by the behaviour of the EoS around $2\times\rho_0$, in contrast to the dominant f/g -mode, which lives primarily at the PNS surface and is determined by bulk PNS parameters. The use of the 2g_1 mode as a probe for the high-density EoS is not limited to the scenario of a first-order phase transition considered in earlier work [73–75]. The signal from the 2g_1 -mode still cannot probe quark formation directly, but may be used to measure the stiffness of the EoS in the aforementioned density regime, which will have implications for the viability of a phase transition or smooth crossover to quark matter. Observations of the 2g_1 -mode feature from a Galactic supernova could thus complement heavy-ion collisions [76] and current astrophysical constraints on the stiffness of the high-density EoS from pulsar masses [77] and NICER data [78, 79] and the GW signal from neutron star mergers. The tidal deformability parameter from the pre-merger GW signal from GW170817 already rules out very stiff EoS [80, 81]. In contrast, recent radius measurements by NICER argue against substantial softening of matter between $2\text{--}3\times\rho_0$ and $4\text{--}5\times\rho_0$ (that would accompany a strong first-order PT in this density regime) [82]. Future work should explore the impact of the EoS and of dimensionality on mode excitation and the signal from the 2g_1 -mode more broadly. Encouragingly, despite generally lower GW amplitudes in three dimensions (3D), the signal has been found in 3D models after submission of our paper [25]. One should also further clarify the physical parameters that govern the mode frequency and power and assess the potential of current and next-generation GW interferometers to detect the signal and reconstruct the trajectory of the mode frequency.

Acknowledgements— The authors are supported by the Australian Research Council (ARC) Centre of Excellence (CoE) for Gravitational Wave Discovery (OzGrav) project number CE170100004. BM is supported by ARC Future Fellowship FT160100035. AH is supported by the ARC CoE for All Sky Astrophysics in 3 Dimensions (ASTRO 3D), through project number CE170100013. JP is supported by the ARC Discovery Early Career Researcher Award (DECRA) project number DE210101050. AM acknowledges the Stern–Gerlach Postdoctoral fellowship and the educator program of the Stiftung Polytechnische Gesellschaft. HS thanks the Walter Greiner Gesellschaft zur Förderung der physikalischen Grundlagenforschung e.V. through the Judah M. Eisenberg Laureatus Chair at the Goethe Universität Frankfurt am Main. We acknowledge computer time allocations from Astronomy Australia Limited’s ASTAC scheme, the National Computational Merit Allocation Scheme (NC-

MAS), and from an Australasian Leadership Computing Grant. Some of this work was performed on the Gadi supercomputer with the assistance of resources and services from the National Computational Infrastructure (NCI), which is supported by the Australian Government. Some of this work was performed on the OzSTAR national facility at Swinburne University of Technology. OzSTAR is funded by Swinburne University of Technology and the National Collaborative Research Infrastructure Strategy (NCRIS). Some of the computational resources were provided by the Goethe-HLR computing center.

* pia.jakobus@monash.edu

- [1] The LIGO Scientific Collaboration, *Classical and Quantum Gravity* **32**, 074001 (2015).
- [2] F. Acernese, M. Agathos, K. Agatsuma, D. Aisa, N. Allemandou, A. Allocca, *et al.*, *Classical and Quantum Gravity* **32**, 024001 (2015).
- [3] H. Abe, T. Akutsu, M. Ando, A. Araya, N. Aritomi, H. Asada, *et al.*, *Galaxies* **10**, 63 (2022).
- [4] B. P. Abbott, R. Abbott, T. D. Abbott, S. Abraham, F. Acernese, Ackley, *et al.*, *Phys. Rev. D* **101**, 084002 (2020).
- [5] V. Kalogera, M.-A. Bizouard, A. Burrows, T. Janka, K. Kotake, Messer, *et al.*, *BAAS* **51**, 239 (2019).
- [6] K. Hayama, T. Kuroda, K. Kotake, and T. Takiwaki, *Phys. Rev. D* **92**, 122001 (2015).
- [7] M. J. Szczepańczyk, J. M. Antelis, M. Benjamin, M. Cavaglià, D. Gondek-Rosińska, T. Hansen, *et al.*, *Phys. Rev. D* **104**, 102002 (2021), arXiv:2104.06462 [astro-ph.HE].
- [8] M. Punturo, M. Abernathy, F. Acernese, B. Allen, N. Andersson, Arun, *et al.*, *Classical and Quantum Gravity* **27**, 194002 (2010).
- [9] M. Szczepańczyk and M. Zanolin, *Galaxies* **10**, 70 (2022).
- [10] J. Powell and B. Müller, *Monthly Notices of the Royal Astronomical Society* **487**, 1178 (2019).
- [11] V. Srivastava, S. Ballmer, D. A. Brown, C. Afle, A. Burrows, D. Radice, and D. Vartanyan, *Phys. Rev. D* **100**, 043026 (2019), arXiv:1906.00084 [gr-qc].
- [12] W. Li, R. Chornock, J. Leaman, A. V. Filippenko, D. Poznanski, Wang, *et al.*, *Monthly Notices of the Royal Astronomical Society* **412**, 1473 (2011), 1006.4613 [astro-ph.SR].
- [13] S. M. Adams, C. S. Kochanek, J. F. Beacom, M. R. Vagins, and K. Z. Stanek, *ApJ* **778**, 164 (2013).
- [14] J. W. Murphy, C. D. Ott, and A. Burrows, *ApJ* **707**, 1173 (2009).
- [15] B. Müller, H.-T. Janka, and A. Marek, *ApJ* **766**, 43 (2013).
- [16] T. Kuroda, T. Takiwaki, and K. Kotake, *Phys. Rev. D* **89**, 044011 (2014).
- [17] T. Kuroda, K. Kotake, and T. Takiwaki, *Astrophysical Journal Letters* **829**, L14 (2016).
- [18] H. Andresen, B. Müller, E. Müller, and H. T. Janka, *Monthly Notices of the Royal Astronomical Society* **468**, 2032 (2017).
- [19] K. N. Yakunin, A. Mezzacappa, P. Marronetti, E. J. Lentz, Bruenn, *et al.*, arXiv e-prints, arXiv:1701.07325

- (2017), arXiv:1701.07325 [astro-ph.HE].
- [20] T. Takiwaki and K. Kotake, Monthly Notices of the Royal Astronomical Society **475**, L91 (2018).
- [21] V. Morozova, D. Radice, A. Burrows, and D. Vartanyan, The Astrophysical Journal **861**, 10 (2018).
- [22] H. Andresen, E. Müller, H. T. Janka, A. Summa, K. Gill, and M. Zanolin, Monthly Notices of the Royal Astronomical Society **486**, 2238 (2019).
- [23] D. Radice, V. Morozova, A. Burrows, D. Vartanyan, and H. Nagakura, The Astrophysical Journal Letters **876**, L9 (2019).
- [24] A. Mezzacappa, P. Marronetti, R. E. Landfield, E. J. Lentz, K. N. Yakunin, Bruenn, *et al.*, Phys. Rev. D **102**, 023027 (2020).
- [25] D. Vartanyan, A. Burrows, T. Wang, M. S. B. Coleman, and C. J. White, Phys. Rev. D **107**, 103015 (2023), arXiv:2302.07092 [astro-ph.HE].
- [26] J. M. Blondin, A. Mezzacappa, and C. DeMarino, ApJ **584**, 971 (2003).
- [27] H. Sotani, T. Kuroda, T. Takiwaki, and K. Kotake, Phys. Rev. D **96**, 063005 (2017).
- [28] A. Torres-Forné, P. Cerdá-Durán, A. Passamonti, and J. A. Font, Monthly Notices of the Royal Astronomical Society **474**, 5272 (2018).
- [29] A. Torres-Forné, P. Cerdá-Durán, A. Passamonti, M. Obergaulinger, and J. A. Font, Monthly Notices of the Royal Astronomical Society **482**, 3967 (2019).
- [30] O. Eggenberger Andersen, S. Zha, A. da Silva Schneider, A. Betranhandy, S. M. Couch, and E. P. O'Connor, ApJ **923**, 201 (2021).
- [31] A. Mezzacappa, P. Marronetti, R. E. Landfield, E. J. Lentz, W. R. Hix, J. A. Harris, *et al.*, arXiv e-prints, arXiv:2208.10643 (2022), arXiv:2208.10643 [astro-ph.SR].
- [32] J. Powell and B. Müller, Phys. Rev. D **105**, 063018 (2022), arXiv:2201.01397 [astro-ph.HE].
- [33] C. Afle, S. K. Kundu, J. Cammerino, E. R. Coughlin, D. A. Brown, D. Vartanyan, and A. Burrows, Phys. Rev. D **107**, 123005 (2023), arXiv:2304.04283 [astro-ph.IM].
- [34] A. Torres-Forné, P. Cerdá-Durán, M. Obergaulinger, B. Müller, and J. A. Font, Phys. Rev. Lett. **123**, 051102 (2019).
- [35] H. Sotani, T. Takiwaki, and H. Togashi, Phys. Rev. D **104**, 123009 (2021).
- [36] N. A. Gentile, M. B. Aufderheide, G. J. Mathews, F. D. Swesty, and G. M. Fuller, ApJ **414**, 701 (1993).
- [37] I. Bednarek, M. Biesiada, and R. Manka, arXiv e-prints, astro-ph/9608053 (1996), arXiv:astro-ph/9608053 [astro-ph].
- [38] I. Sagert, T. Fischer, M. Hempel, G. Pagliara, J. Schaffner-Bielich, A. Mezzacappa, Thielemann, *et al.*, Phys. Rev. Lett. **102**, 081101 (2009).
- [39] T. Fischer, N.-U. F. Bastian, M.-R. Wu, P. Baklanov, E. Sorokina, S. Blinnikov, *et al.*, Nature Astronomy **2**, 980 (2018).
- [40] V. Dexheimer, L. T. T. Soethe, J. Roark, R. O. Gomes, S. O. Kepler, and S. Schramm, Int. J. Mod. Phys. E **27**, 1830008 (2018), arXiv:1901.03252 [astro-ph.HE].
- [41] E. R. Most, L. J. Papenfort, V. Dexheimer, M. Hanauske, S. Schramm, H. Stöcker, and L. Rezzolla, Phys. Rev. Lett. **122**, 061101 (2019).
- [42] A. Bauswein, N.-U. F. Bastian, D. B. Blaschke, K. Chatziioannou, J. A. Clark, T. Fischer, and M. Oertel, Phys. Rev. Lett. **122**, 061102 (2019).
- [43] M. Hanauske, L. Bovard, E. Most, J. Papenfort, J. Steinheimer, M. A., *et al.*, Universe **5**, 156 (2019).
- [44] N. Yasutake, K. Kotake, M.-A. Hashimoto, and S. Yamada, Phys. Rev. D **75**, 084012 (2007).
- [45] S. Zha, E. P. O'Connor, M.-c. Chu, L.-M. Lin, and S. M. Couch, Phys. Rev. Lett. **125**, 051102 (2020).
- [46] T. Kuroda, T. Fischer, T. Takiwaki, and K. Kotake, ApJ **924**, 38 (2022).
- [47] A. W. Steiner, M. Hempel, and T. Fischer, ApJ **774**, 17 (2013).
- [48] A. Motornenko, J. Steinheimer, V. Vovchenko, S. Schramm, and H. Stoecker, Phys. Rev. C **101**, 034904 (2020).
- [49] B. Müller, H.-T. Janka, and H. Dimmelmeier, ApJS **189**, 104 (2010).
- [50] B. Müller and H. T. Janka, MNRAS **448**, 2141 (2015).
- [51] L. S. Finn, in *Frontiers in Numerical Relativity*, edited by C. R. Evans, L. S. Finn, and D. W. Hobill (1989) pp. 126–145.
- [52] T. A. Weaver, G. B. Zimmerman, and S. E. Woosley, ApJ **225**, 1021 (1978).
- [53] A. Heger and S. E. Woosley, ApJ **724**, 341 (2010).
- [54] E. R. Most, A. Motornenko, J. Steinheimer, V. Dexheimer, M. Hanauske, L. Rezzolla, *et al.*, arXiv e-prints, arXiv:2201.13150 (2022), arXiv:2201.13150 [nucl-th].
- [55] P. Jakobus, B. Müller, A. Heger, A. Motornenko, J. Steinheimer, and H. Stoecker, MNRAS **516**, 2554 (2022).
- [56] J. Morlet, G. Arens, I. Forgeau, and D. Giard, Geophysics **47**, 203 (1982).
- [57] A. Marek, H. T. Janka, and E. Müller, Astronomy and Astrophysics **496**, 475 (2009).
- [58] K. N. Yakunin, P. Marronetti, A. Mezzacappa, S. W. Bruenn, C.-T. Lee, Chertkow, *et al.*, Classical and Quantum Gravity **27**, 194005 (2010).
- [59] P. Cerdá-Durán, N. DeBrye, M. A. Aloy, J. A. Font, and M. Obergaulinger, ApJ **779**, L18 (2013).
- [60] H. Kawahara, T. Kuroda, T. Takiwaki, K. Hayama, and K. Kotake, ApJ **867**, 126 (2018).
- [61] D. E. Myers, WIT Transactions on Modelling and Simulation **23** (1970).
- [62] S. Altiparmak, C. Ecker, and L. Rezzolla, ApJ **939**, L34 (2022), arXiv:2203.14974 [astro-ph.HE].
- [63] Y. Fujimoto, K. Fukushima, and K. Murase, Phys. Rev. D **101**, 054016 (2020), arXiv:1903.03400 [nucl-th].
- [64] S. Soma, L. Wang, S. Shi, H. Stöcker, and K. Zhou, Phys. Rev. D **107**, 083028 (2023).
- [65] M. Omana Kuttan, J. Steinheimer, K. Zhou, and H. Stoecker, arXiv e-prints, arXiv:2211.11670 (2022), arXiv:2211.11670 [nucl-th].
- [66] D. Oliinychenko, A. Sorensen, V. Koch, and L. McLerran, Phys. Rev. C **108**, 034908 (2023).
- [67] H. Nagakura, A. Burrows, D. Radice, and D. Vartanyan, Monthly Notices of the Royal Astronomical Society **492**, 5764 (2020).
- [68] S. W. Bruenn and T. Dineva, ApJ **458**, L71 (1996).
- [69] S. W. Bruenn, E. A. Raley, and A. Mezzacappa, arXiv e-prints, astro-ph/0404099 (2004).
- [70] R. Glas, H. T. Janka, T. Melson, G. Stockinger, and O. Just, ApJ **881**, 36 (2019).
- [71] B. Müller, Living Reviews in Computational Astrophysics **6**, 3 (2020).
- [72] L. F. Roberts, G. Shen, V. Cirigliano, J. A. Pons,

- S. Reddy, and S. E. Woosley, *Phys. Rev. Lett.* **108**, 061103 (2012).
- [73] P. N. McDermott, *Monthly Notices of the Royal Astronomical Society* **245**, 508 (1990).
- [74] T. E. Strohmayer, *ApJ* **417**, 273 (1993).
- [75] G. Miniutti, J. A. Pons, E. Berti, L. Gualtieri, and V. Ferrari, *MNRAS* **338**, 389 (2003), arXiv:astro-ph/0206142 [astro-ph].
- [76] S. Huth, P. T. H. Pang, I. Tews, T. Dietrich, A. Le Fèvre, A. Schwenk, W. Trautmann, K. Agarwal, M. Bulla, M. W. Coughlin, and C. Van Den Broeck, *Nature* **606**, 276 (2022).
- [77] P. B. Demorest, T. Pennucci, S. M. Ransom, M. S. E. Roberts, and J. W. T. Hessels, *Nature* **467**, 1081 (2010).
- [78] T. E. Riley, A. L. Watts, P. S. Ray, S. Bogdanov, S. Guillot, Morsink, *et al.*, *ApJ* **918**, L27 (2021).
- [79] M. C. Miller, F. K. Lamb, A. J. Dittmann, S. Bogdanov, Z. Arzoumanian, Gendreau, *et al.*, *ApJ* **918**, L28 (2021).
- [80] B. P. Abbott *et al.* (LIGO Scientific Collaboration and Virgo Collaboration), *Phys. Rev. Lett.* **116**, 061102 (2016).
- [81] B. P. Abbott, R. Abbott, T. D. Abbott, F. Acernese, K. Ackley, C. Adams, *et al.* (The LIGO Scientific Collaboration and the Virgo Collaboration), *Phys. Rev. Lett.* **121**, 161101 (2018).
- [82] T. Kojo, G. Baym, and T. Hatsuda, *ApJ* **934**, 46 (2022).

Supplementary Material:
**Gravitational Waves from a Core g-Mode in Supernovae as Probes of the
High-Density Equation of State**

Pia Jakobus,* Bernhard Müller, and Alexander Heger
School of Physics and Astronomy, Monash University, Clayton, VIC 3800 Australia

Shuai Zha
Tsung-Dao Lee Institute, Shanghai Jiao Tong University, Shanghai 200240, China

Jade Powell
Centre for Astrophysics and Supercomputing, Swinburne University of Technology, Hawthorn, VIC 3122, Australia

Anton Motornenko, Jan Steinheimer, and Horst Stoecker
Frankfurt Institute for Advanced Studies, Giersch Science Center, Frankfurt am Main, Germany

(Dated: October 3, 2023)

arXiv:2301.06515v2 [astro-ph.HE] 1 Oct 2023

* pia.jakobus@monash.edu

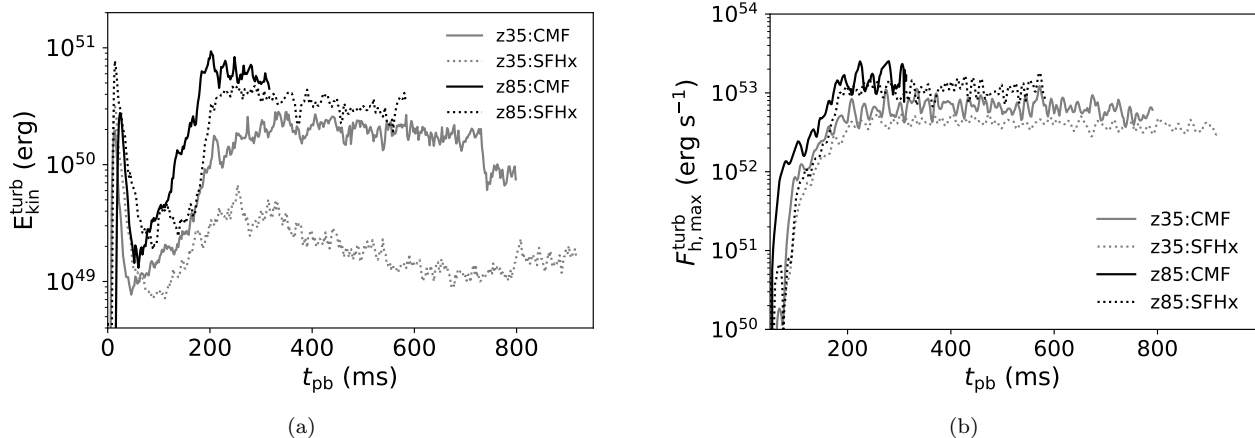


FIG. 1: (a) Turbulent kinetic energy of the PCS as function of post-bounce time for the progenitors z35 (grey) and z85 (black) using the SFHx EoS (dashed lines) and CMF EoS (solid lines). (b) Maximal turbulent energy flux $F_{\text{conv,max}}^{\text{h}}$ in the PCS convection zone (time averaged over 10 ms) for all four models as a function of post-bounce time. The same line styles as in Panel (a) are used.

I. TURBULENT KINETIC ENERGY IN THE CONVECTION ZONE

We define the turbulent kinetic energy in terms of the turbulent velocity fluctuations δv and the density ρ as

$$E_{\text{kin}}^{\text{turb}} = \frac{1}{2} \int_{\text{PCS}} \delta v^2 \rho dV, \quad (1)$$

where the volume element dV includes the appropriate relativistic metric factors¹, i.e., $dV = 2\pi\phi^6 r^2 \sin\theta dr d\theta$ in axisymmetry with the conformal factor ϕ . The integral is performed over the entire proto-compact star (PCS), i.e., for densities above $10^{11} \text{ g cm}^{-3}$. The turbulent velocity fluctuations are given by

$$\delta v^2 = (v_r - \langle v_r \rangle)^2 + v_\theta^2, \quad (2)$$

where $\langle v_r \rangle$ is the spherical Favre average of the radial velocity.

We plot $E_{\text{kin}}^{\text{turb}}$ for all four models as function of time in Figure 1. The CMF models show higher turbulent kinetic energies compared to the SFHx models, especially for the lighter z35 progenitor. In this case, the turbulent kinetic energy in the PCS convection zone is about an order of magnitude higher in the CMF EoS compared to SFHx. For z85, the difference is modest but robust, and the rise of the turbulent kinetic energy to the plateau at $\sim 5 \times 10^{50}$ erg occurs significantly earlier.

In addition, we consider the turbulent energy flux as

$$F_{\text{turb}}^{\text{h}} = 4\pi r^2 \langle \rho v_r'' h'' \rangle \quad (3)$$

$$= 4\pi r^2 \int \alpha \phi^4 \rho v_r'' h'' r^2 d\Omega, \quad (4)$$

where $X'' = X - \langle X \rangle$, with the Favre average $\langle X \rangle$. α is the lapse function. The behaviour of the turbulent flux is similar to the turbulent kinetic energy: z85:CMF exhibits the largest flux, followed by z85:SFHx, and z35:CMF. The progenitor z35:SFHx exhibits a notably lower flux, although the difference in comparison to z35:CMF is relatively smaller than what is observed for the turbulent kinetic energy in the left plot of Fig. 1. High peak values are reached by this metric for the strength of convection i) because the neutrino losses that drive convection are unusually for these high mass progenitors, and ii) because this metric is sensitive to considerable fluctuations in the profiles of the turbulent energy flux in 2D simulations.

¹ The deviation of the Lorentz factor from unity is negligible in the proto-compact star because the fluid velocities are small.

II. ELECTRON FRACTION GRADIENT

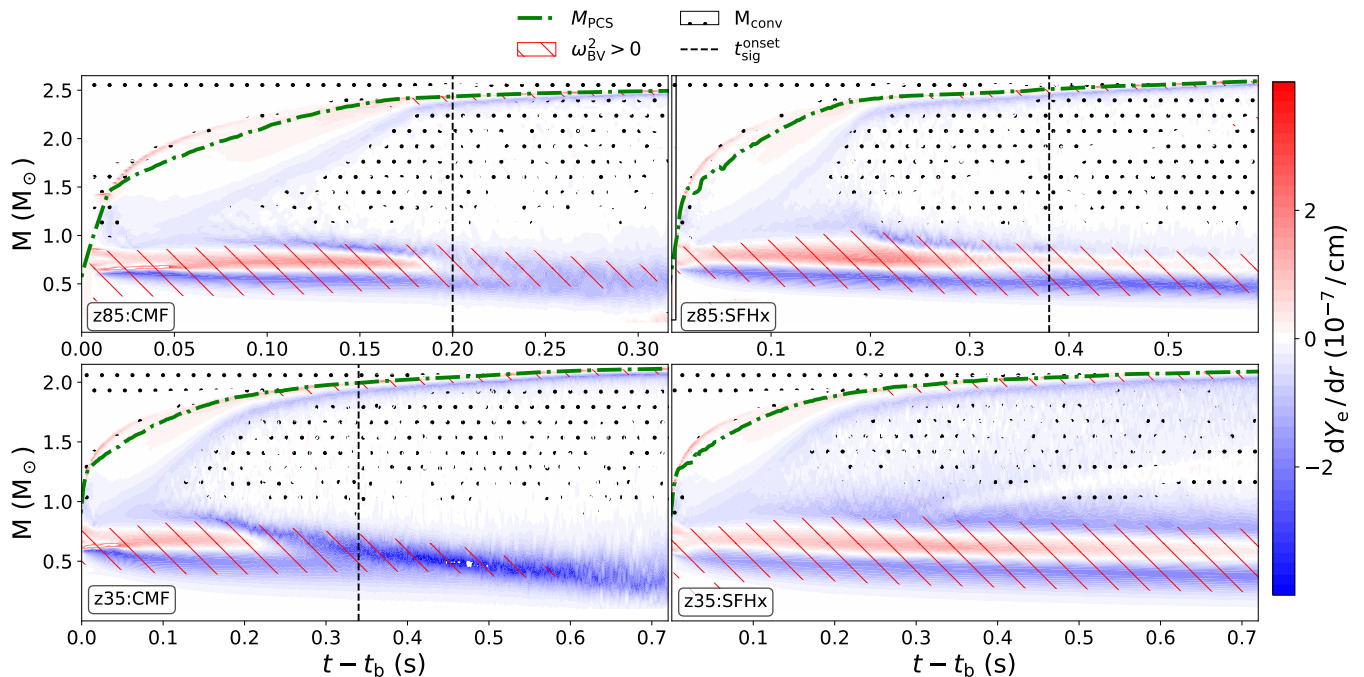


FIG. 2: Evolution of the gradient dY_e/dr of the spherically-averaged electron fraction as function of post-bounce time for the CMF model (left), SFHx (right) for z85 (upper panel) and z35 (lower panel). The black circles approximately track the PCS convection zone. Red dashes show buoyantly stable regions where $\omega_{\text{BV}}^2 > 0$. Those areas are susceptible to quadrupolar perturbations at the frequency of the g_1^2 -mode. The black-dashed vertical line roughly corresponds to the onset of the g_1^2 -signal in the GW spectrograms.

The differences in the Brunt-Väisälä frequency in the region below the PCS convection zone in the various models affect the frequency of the g_1^2 -mode and may also have some bearing on its excitation by turbulent motions in the overlying convection zone. Aside from the different sound speed above nuclear saturation density, differences in the Brunt-Väisälä frequency between the CMF and SFHx models also arise because the electron fraction evolves differently during the post-bounce phase. To illustrate this effect we show the gradient of the spherically-averaged electron fraction.

Initially, all models show a slight negative electron fraction gradient in the PCS core inside $\sim 0.7 M_\odot$ (inner blue region in Figure 2), and then a small “hump” that is visible as a red stripe and blue stripe further outside in Figure 2. With time, neutrino diffusion erases the hump, and the two blue regions merge in the CMF models. This process takes considerably longer in model z85:SFHx, and in model z85:SFHx the hump is still clearly present at the end of the simulation. The evolution of the electron fraction hump in the code is affected by a combination of factors that determine the neutrino opacities in this region, i.e., density, temperature, and neutron, proton, and neutrino chemical potentials. Hence there is no straightforward explanation for the faster disappearance of the hump in the CMF models at this time.

III. DECOMPOSITION OF TERMS CONTRIBUTING TO THE BRUNT-VÄISÄLÄ FREQUENCY

To elucidate how differences in the entropy and electron fraction gradients and various thermodynamic derivatives affect the Brunt-Väisälä frequency at the inner boundary of the PCS convection zone, we rewrite the relativistic Brunt-Väisälä frequency as

$$\omega_{\text{BV}}^2 = \frac{d\alpha}{dr} \frac{\alpha}{\rho h \phi^4} \frac{1}{c_s^2} \left[\left(\frac{\partial P}{\partial s} \right)_{\tilde{\rho}, Y_e} \frac{ds}{dr} + \left(\frac{\partial P}{\partial Y_e} \right)_{\tilde{\rho}, s} \frac{dY_e}{dr} \right]. \quad (5)$$

Here, α is the lapse function, ϕ is the conformal factor, ρ is the baryonic mass density, $\tilde{\rho}$ is the total mass-energy density, P is the pressure, $h = (\tilde{\rho} + P/c^2)/\rho$ is the relativistic enthalpy, s is the specific entropy per baryon, Y_e is the lepton fraction, and c_s^2 is the (adiabatic) sound speed².

The individual terms in Equation (5) and their products are plotted in Figure 4 for the z85 models and in Figure 3 for the z35 models. Each figure shows the results for the CMF models (solid lines) and the SFHx models (dotted) at 4 different times.

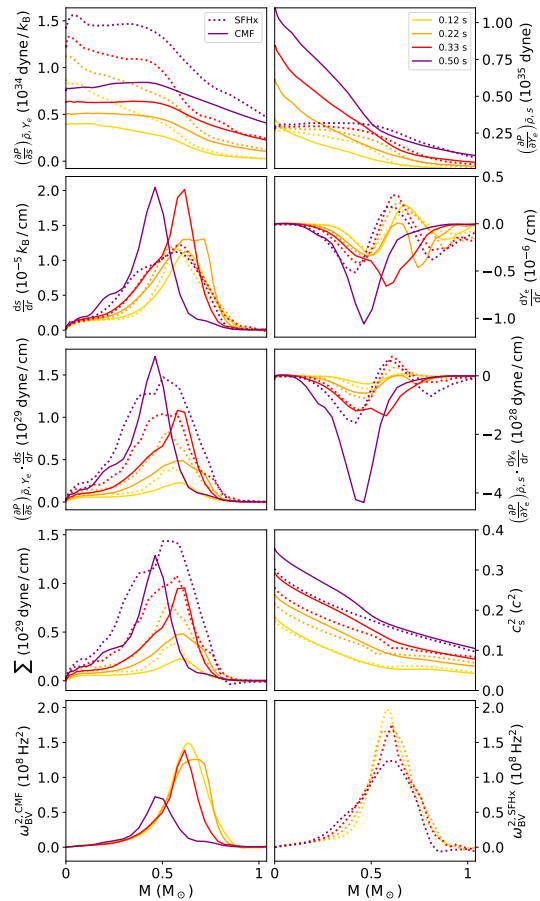


FIG. 3: Individual terms in Equation (5) for z35:CMF (solid lines) and z35:SFHx (dotted) at four different post-bounce times. The left panel in the fourth row shows the term in square brackets of Equation 5, i.g. $\sum \equiv \left(\frac{\partial P}{\partial s} \right)_{\tilde{\rho}, Y_e} \frac{ds}{dr} + \left(\frac{\partial P}{\partial Y_e} \right)_{\tilde{\rho}, s} \frac{dY_e}{dr}$.

² Note that the small effect of neutrino pressure and energy density is not included in Equation (5).

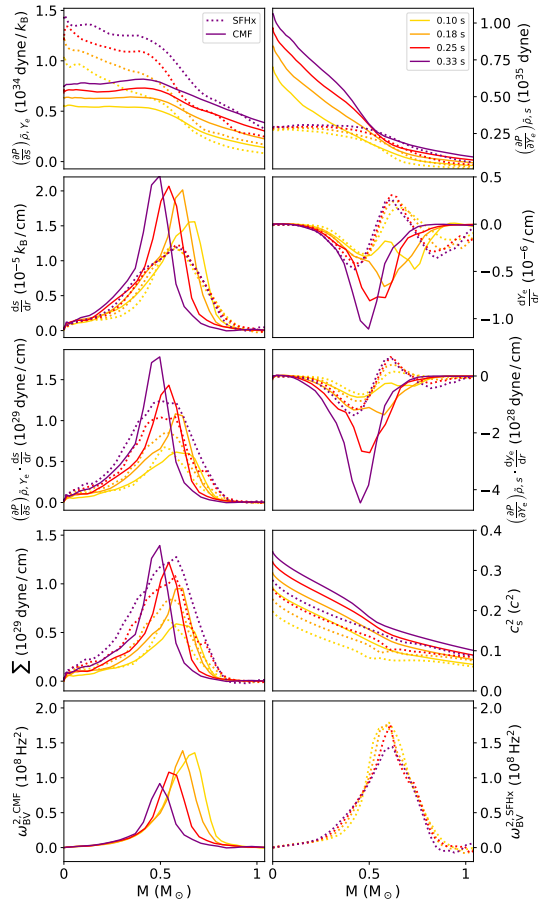


FIG. 4: Individual terms for **z85:CMF** (solid lines) and **z85:SFHx** (dotted) at four different post-bounce times. See Figure 3.

The figures show that $\left(\frac{\partial P}{\partial s}\right)_{\bar{\rho}, Y_e}$ and $\frac{ds}{dr}$ are quite different for the CMF and SFHx models, but the product $\left(\frac{\partial P}{\partial s}\right)_{\bar{\rho}, Y_e} \frac{ds}{dr}$ is rather similar. The electron fraction gradient becomes steeper in the CMF models, which pushes the Σ -term in square brackets in Equation (5),

$$\Sigma = \left(\frac{\partial P}{\partial s}\right)_{\bar{\rho}, Y_e} \frac{ds}{dr} + \left(\frac{\partial P}{\partial Y_e}\right)_{\bar{\rho}, s} \frac{dY_e}{dr}$$

to slightly lower values, compared to **z85:SFHx** where the radial profile of $\left(\frac{\partial P}{\partial Y_e}\right)_{\bar{\rho}, s} \frac{dY_e}{dr}$ is flatter and largely positive. The effect is less pronounced for the more massive progenitor **z85:CMF**; the Σ -term here is dominated by a larger entropy gradient. For both progenitors, **z85** and **z35**, the sound speed in the region below the PCS convection zone is increasingly higher in the CMF models, which systematically pushes ω_{BV} to lower values. In the case of model **z85**, this effect explains the difference in the Brunt-Väisälä frequency, as the Σ -term is similar for the SFHx and CMF EoS.

IV. RADIALLY RESOLVED GW SIGNALS

For completeness, we show plots analogously to Figure 2 in the main text. Figures 5, 6, and 7 present the results for model **z85:CMF**, **z85:SFHx**, and **z35:SFHx** respectively. The figures show the radius- and frequency-dependent amplitude $\tilde{q}(r, f)$ of quadrupolar perturbations (first two panels from the left) for two different time intervals Δt_1 and Δt_2 , which are indicated in the third panel by black and red dash-dotted vertical lines. The third panels also show the quark fraction (background color; only present in Figure 5) and the adiabatic index (contour lines). The fourth panel shows the squared Brunt-Väisälä frequency and the spherically averaged specific entropy per baryon.

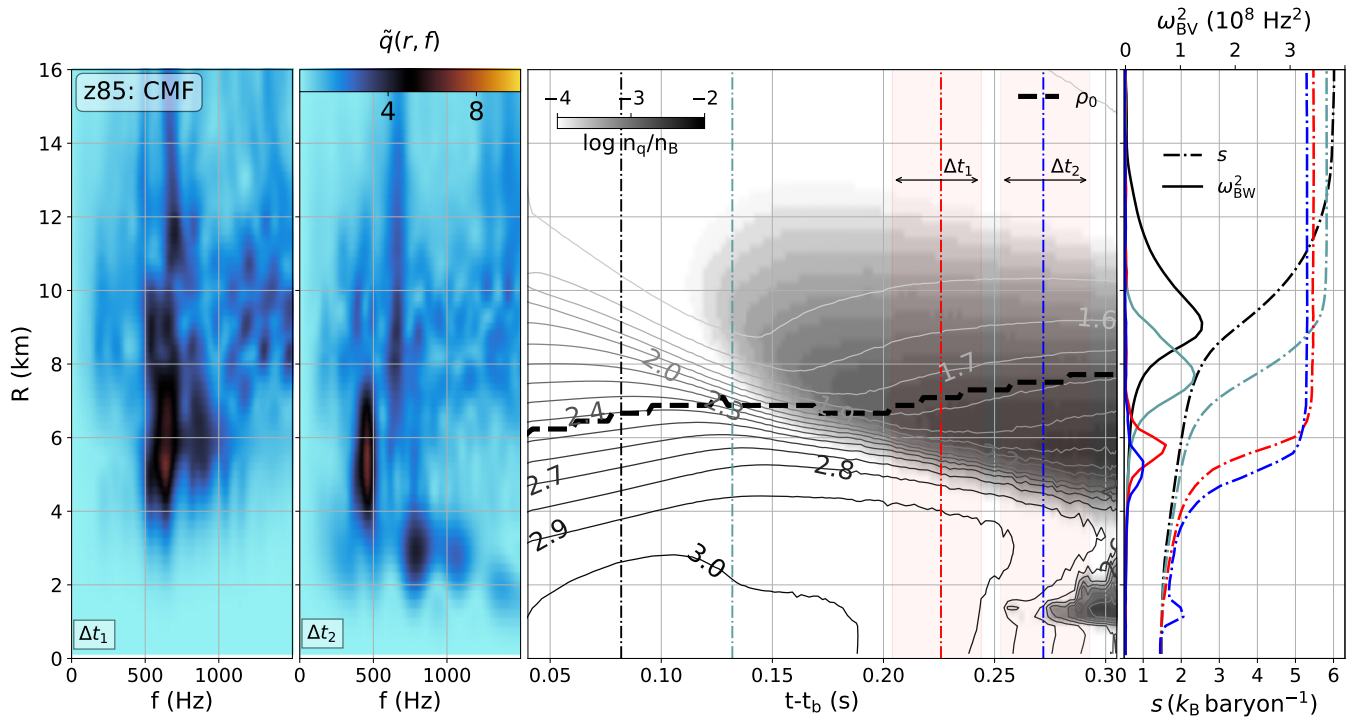


FIG. 5: Quadrupolar perturbations, quark fraction, adiabatic index, Brunt-Väisälä frequency and spherically averaged entropy for model z85:CMF; see detailed description in text.

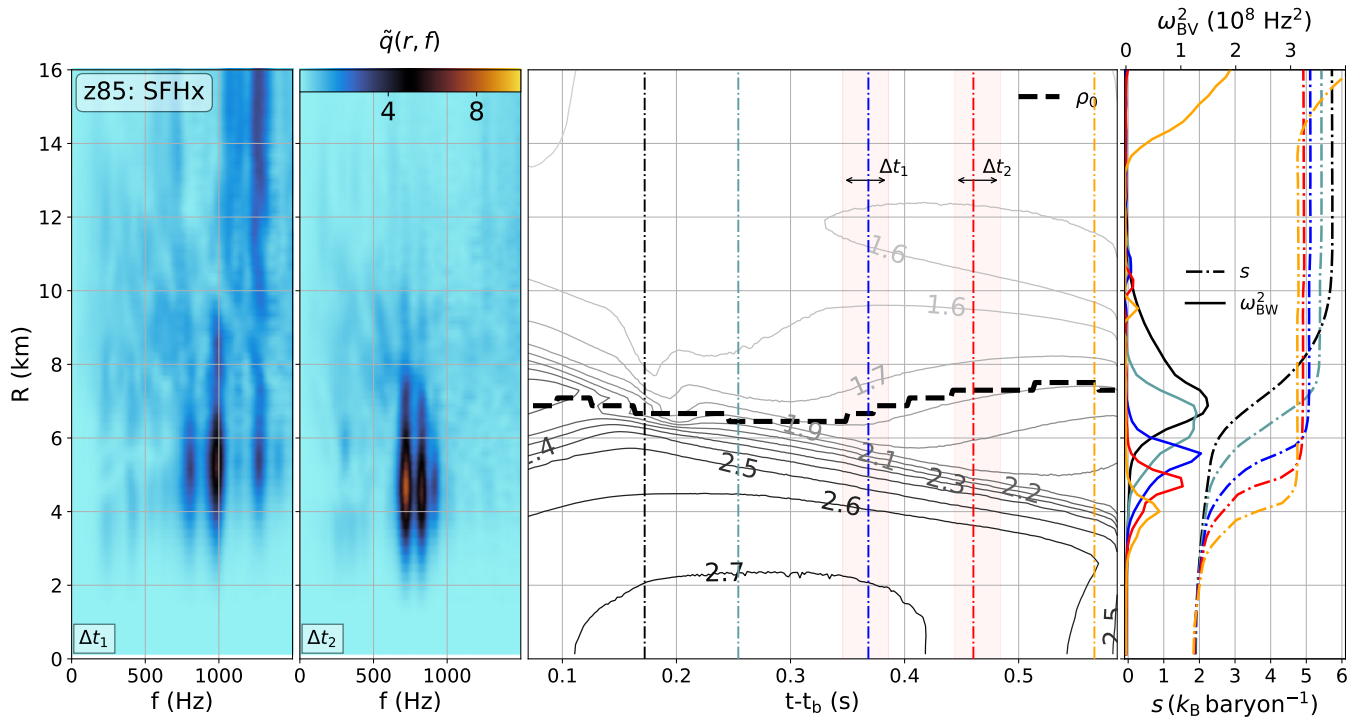


FIG. 6: Quadrupolar perturbations, adiabatic index, Brunt-Väisälä frequency and spherically averaged entropy for model z85:SFHx; see detailed description in text. Note that the SFHx EoS is purely hadronic.

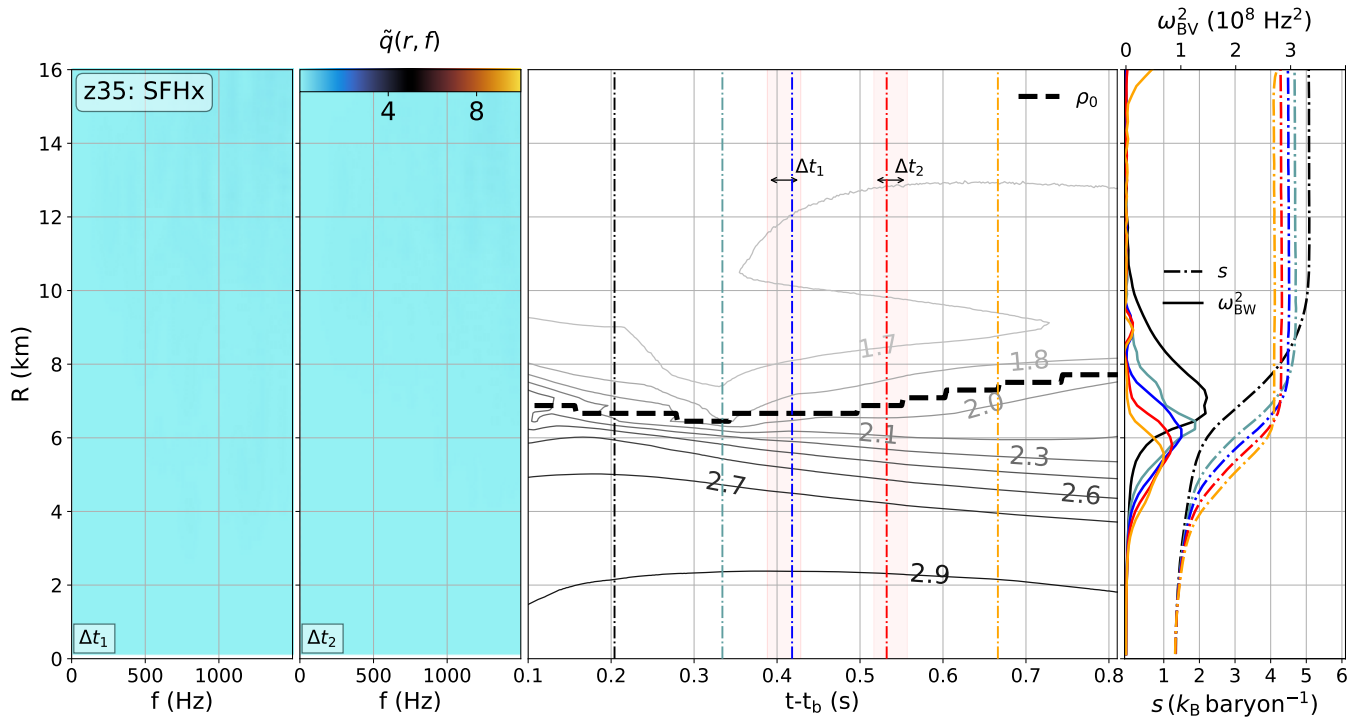


FIG. 7: Analogously to Figure 6 but for model z35:SFHx where no signal is observed.